Biochimica et Biophysica Acta 1847 (2015) 343–354

Contents lists available at ScienceDirect

Biochimica et Biophysica Acta

journal homepage: www.elsevier.com/locate/bbabio

Time-resolved visible and infrared difference spectroscopy for the study of photosystem I with different quinones incorporated into the A1 binding site

Hiroki Makita, Nan Zhao, Gary Hastings *

Department of Physics and Astronomy, Georgia State University, Atlanta, GA 30303, USA

ARTICLE INFO

Article history:
Received 9 July 2014
Received in revised form 12 December 2014
Accepted 15 December 2014
Available online 19 December 2014

Keywords:
Photosystem I
Time resolved
A1
Phylloquinone
Electron transfer
FTIR

ABSTRACT

Room (298 K) and low (77 K) temperature time-resolved visible and infrared difference spectroscopy has been used to study photosystem I particles with phylloquinone (2-methyl-3-phytyl-1,4-naphthoquinone), menadione (2-methyl-1,4-naphthoquinone) and plastoquinone 9 (2,3-dimethyl-5-prenyl-l,4-benzoquinone), incorporated into the A_1 binding site. Concentrated samples in short path-length (~5 μm) sample cells are typically used in FTIR experiments. Measurements were undertaken using standard "dilute" samples at 298 K, and concentrated (~5×) samples at both 298 and 77 K. No concentration induced alterations in the flash-induced absorption changes were observed. Concentrated samples in short path-length cells form a transparent film at 77 K, and could therefore be studied spectroscopically at 77 K without addition of a cryoprotectant. At 298 K, for photosystem I with plastoquinone 9/menadione/phylloquinone incorporated, $P700^+F_{A/B}^-$ radical pair recombination is characterized by a time constant of 3/14/80 ms, and forward electron transfer from A_{1A}^- to F_x by a time constant of 211/3.1/0.309 μs, respectively. At 77 K, for concentrated photosystem I with menadione/phylloquinone incorporated, $P700^+A_1^-$ radical pair recombination is characterized by a time constant of 240/340 μs, with this process occurring in 58/39% of the PSI particles, respectively. The origin of these differences is discussed. Marcus electron transfer theory in combination with kinetic modeling is used to simulate the observed electron transfer time constants at 298 K. This simulation allows an estimate of the redox potential for the different quinones in the A_1 binding site.

1. Introduction

In photosynthetic oxygen evolving organisms solar energy is captured and converted independently, but cooperatively, in two separate photosystems called photosystem I and photosystem II. Photosystem II uses light to catalyze the generation of products that eventually lead to the oxidation of water and the subsequent liberation of molecular oxygen as a by-product. Photosystem I (PSI) on the other hand uses light to catalyze the formation of reducing products that eventually leads to the reduction of carbon dioxide, and its eventual incorporation into glucose.

In each of the two photosystems light energy conversion is realized via the transfer of electrons via a series of protein bound acceptors across a biological membrane. The nature of the acceptors in terms of their electronic and structural organization within the protein environment has been a subject of interest for decades.

In this manuscript we focus on photosystem I (PSI) reaction centers (RCs). More specifically, we focus on the quinone molecule that occupies the A_1 binding site in cyanobacterial PSI particles from *Synechocystis* sp. 6803 (*S6803*). The arrangement of the electron transfer (ET) cofactors in the PSI RC is outlined in Fig. 1A. PSI contains two almost identical chains of ET cofactors bound to the protein subunits PsaA or PsaB. The cofactors bound to the PsaA or PsaB proteins are labeled with a subscript A or B, respectively. P700, the primary electron donor in PSI, is a heterodimeric Chl-*a*/Chl-*a*′ species, where Chl-*a*′ is a 13^2 epimer of Chl-*a* [1]. The primary electron acceptor, A_0, is a monomeric Chl-*a* molecule [2], and A_1 is a phylloquinone (PhQ) molecule [3]. PhQ is a 2-methyl-3-phytyl-1,4-naphthaquinone, the structure of which is outlined in Fig. 1B. F_X, F_A and F_B are (4Fe–4S) iron sulfur clusters [4,5].

In PSI, following light excitation of P700, an electron is transferred to A_1 (via A_0) in <50 ps [6,7]. To further stabilize the charge separated state, the electron is then transferred from A_1^- to F_X. A_1^- to F_X ET is characterized by two time constants of 10–25 ns and 260–340 ns at room temperature (RT) [8–12]. From F_X^- an electron is then transferred to F_A and F_B, also on a nanosecond timescale [13].

Abbreviations: 2MNQ, 2-methyl, 1,4-naphthquinone (menadione/vitamin k_3); Chl-a, chlorophyll-a; DS, difference spectra, spectrum, spectroscopy or spectroscopic; DDS, double difference spectrum; C = O, carbonyl; ET, electron transfer; FTIR, Fourier transform infrared; H bond, hydrogen bond; ms, millisecond; ns, nanosecond; PhQ, phylloquinone (vitamin k_1); PQ_9, plastoquinone 9; PSI, photosystem I; RC, reaction center; RT, room temperature; *S6803*, *Synechocystis* sp. 6803; TR, time resolved

* Corresponding author. Tel.: +1 404 413 6055.
E-mail address: ghastings@gsu.edu (G. Hastings).

http://dx.doi.org/10.1016/j.bbabio.2014.12.007
0005-2728/

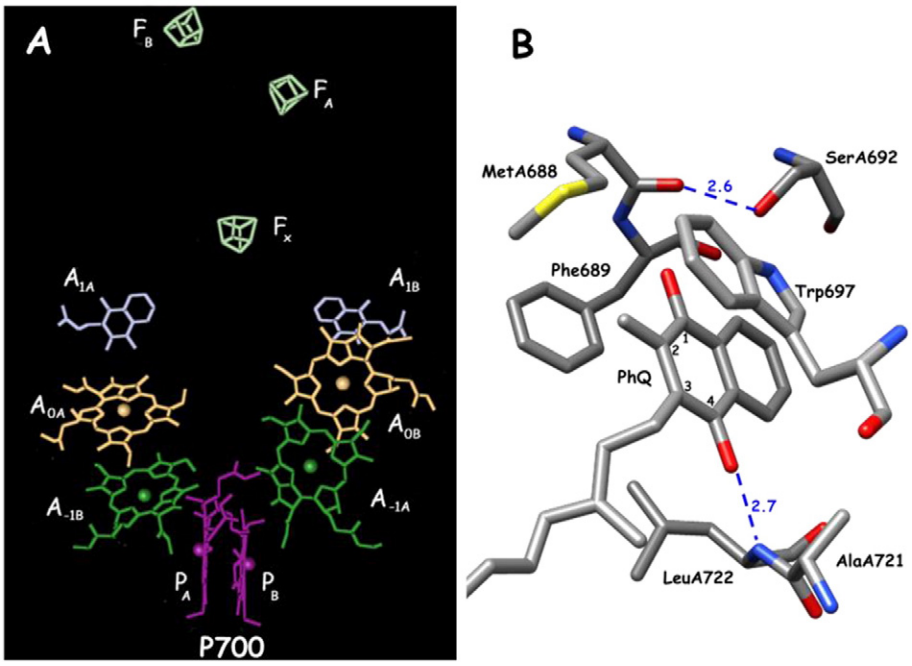

Fig. 1. (A) Arrangement of the two branches of ET cofactors in PSI. Number subscript refers to cofactor. Letter subscript refers to protein subunit (PsaA or B) to which cofactor is bound. The A/B-branch refers to the set of ET cofactors on the left/right side, respectively. Fig. 1A is generated using the 2.5 Å x-ray crystal structure of trimeric PSI particles from the cyanobacterium *Synechococcus elongatus* (PDB file accession number PDB ID: 1JB0) [5]. (B) View of PhQ in the A_{1A} binding site. Possible H-bonding interactions are shown (*dotted*), and PhQ numbering scheme is indicated. Nitrogen/oxygen/sulfur atoms are blue/red/yellow, respectively.

As mentioned, in cyanobacterial PSI at RT, forward ET from A_1^- to F_X is characterized by two phases with time constants of 10–25 ns and 260–340 ns [8–12]. These "fast" and "slow" kinetic phases have been associated with ET down the B and A branches, respectively [8–12]. As the temperature is lowered, in a portion of the RCs, forward ET diminishes and is replaced by a $P700^+A_1^-$ direct recombination reaction, which is characterized by a time constant of ~245 μs at 77 K [8]. This time constant is found using PSI particles from *Synechococcus elongatus*. In PSI from *S6803* the corresponding time constant is ~285–340 μs (see below and [9]). In cyanobacterial PSI particles at 77 K, the $P700^+A_1^-$ state recombines in ~45% of the particles, the $P700^+F_X^-$ state recombines in greater than 5 ms in ~20% of the PSI particles, and in ~35% of the PSI particles ET is irreversible [8]. The degree to which each branch is active in ET is becoming clearer [14,15], with the 260–340 ns/285–340 μs components at RT/77 K, respectively, being associated with ET along the A branch [14–16]. The 10–25 ns phase and the irreversible fraction at RT and 77 K, respectively, have been associated with ET along the B branch [16,17]. The different rates of ET from A_1^- to F_X at RT, as well as the different functionality at 77 K is primarily ascribed to different midpoint potentials of PhQ in the A_1 binding site on the A and B branches.

The reported range of the midpoint potential for PhQ occupying the A_1 binding site is −670 to −850 mV (see [16] for a review), making it one of the most reducing quinones in biology. The estimated difference in the midpoint potentials between A_{1A} and A_{1B} ranges from 25 to 173 mV, with ET from A_{1A}^- to F_X being "thermodynamically uphill" while A_{1B}^- to F_X is "thermodynamically downhill" [17,18] (see below).

The unprecedented redox potential of PhQ in the A_1 binding site is in part a result of interactions of PhQ with the surrounding protein environment. Fig. 1B shows a view of PhQ in the A_{1A} binding site and several of the surrounding amino acids. The B-side is similar. Fig. 1B indicates that the C_1=O group of PhQ is not H-bonded whereas the C_4=O is H-bonded to the backbone NH group of LeuA722 (*S. elongatus* numbering).

Recently it has been demonstrated that different quinones can be incorporated into the A_1 binding site in *menB* null mutant PSI particles simply by incubating the particles in a large molar excess of the quinone of interest [19–22]. This quinone incubation method relies on mutant cells (from the cyanobacterium *Synechocystis* sp. 6803) in which genes that code for enzymes involved in PhQ biosynthesis have been disrupted [23,24]. For example, in mutants where the *menB* gene has been deactivated PhQ biosynthesis is inhibited and plastoquinone-9 (PQ_9) is recruited into the A_1 site instead [23–25]. PSI particles from these mutant cells will be referred to as $menB^-$ PSI particles. In $menB^-$ PSI particles foreign quinones can displace PQ_9 in the A_1 binding site, simply by incubating particles in the presence of the quinone of interest [19–22].

In this manuscript we describe work undertaken using regular $menB^-$ PSI particles, with PQ_9 in the A_1 binding site, and $menB^-$ PSI particles with PhQ or menadione [2-methyl-1,4-naphthquinone (2MNQ)] incorporated into the A_1 binding site. This manuscript focuses on measurement of the kinetics of forward and reverse ET in PSI samples with the three different quinones incorporated, at both RT and 77 K. The kinetics of ET are sensitive to the redox potential of the quinone in the A_1 binding site, and here we use Marcus theory in combination with a quasi-equilibrium model (of radical pair states) to estimate the redox potentials of the quinones in the A_1 binding site.

2 . Materials and methods

Trimeric PSI particles from *menB* null mutant cells from *Synechocystis* sp. PCC 6803 (*S6803*) were isolated and stored as described previously [23]. To incorporate quinones into the A_1 binding site, PSI particles are incubated in the presence of a ~1000× molar excess of the quinone of interest (quinone/RC ratio). Quinones were dissolved in ethanol and added in such a way that the ethanol concentration never exceeds 2% of the total volume. PSI particles were

incubated in the presence of quinone at 4 °C in the dark for ~24 h, with stirring. Alternatively, PSI particles could be incubated at RT with stirring for 4 h.

2.1. Time-resolved absorption spectroscopy in the visible spectral range

Nanosecond (ns) to millisecond (ms) transient absorption spectroscopy in the visible spectral region was undertaken using an Edinburgh Instruments LP920 flash photolysis spectrometer. 532 nm, 5 ns pulses from a Continuum Minilite Nd:YAG laser were used for excitation. A flash repetition rate of 10 Hz was typically used, although measurements at 1 or 0.2 Hz were found to yield similar results (not shown). A xenon arc lamp was used as probe light source in either CW mode (for measurements over tens of milliseconds) or pulsed mode (for temporal changes on a timescale less than 1 ms). In pulsed mode the xenon arc lamp produces flashes of ~2 ms duration with a relatively flat intensity profile over most of this range. A 1 cm water cell was placed in front of the probe lamp to reduce heating effects.

Flash-induced absorption changes were measured at 800, 703 and 487 nm. After passing through the sample, probing light was directed through a monochromator (Bentham Instruments TMc 300) to select the probe wavelength. Probe light was detected using a Hamamatsu R928 photomultiplier tube. To minimize actinic effects of the probing light narrow-band (10 nm FWHM) interference filters were placed in front of the sample. Optical filters were also placed after the sample, in front of the entrance slit to the monochromator, in order to attenuate 532 nm laser scattered photons.

2.2. Time-resolved step-scan FTIR

Time-resolved step-scan FTIR experiments with 6 μs time resolution, at 77 K, were undertaken as described previously [26–28]. Data were collected in the 1950–1100 cm^{-1} region at 4 cm^{-1} spectral resolution. For time-resolved step-scan FTIR measurements PSI samples are concentrated to a thick paste and then squeezed between two calcium fluoride windows. The windows were pressed until the sample has an amide II absorbance (at ~1550 cm^{-1}) of ~0.8 at RT. The path-length in the sample cells is estimated to be <5 μm. Samples were mounted in a cryostat (APD cryogenics or Cryo Industries of America) and the temperature was lowered to 77–81 K (hereafter referred to as 77 K).

PSI samples used in FTIR measurements formed a clear glass at both RT and 77 K. Both visible and infrared measurements were undertaken using the same sample, in the same sample cell, without cryoprotectant. Samples prepared for FTIR spectroscopy have very high absorption in the visible region, with the OD at the peak of the Q_y absorption band (at ~679 nm) being greater than 5.0. The sample OD at 703 and 800 nm is still well below 1.0, so probing at these wavelengths is still feasible. So for samples used in FTIR measurements, time-resolved visible measurements probing at 703 and 800 nm, at both RT and 77 K were undertaken. For samples prepared for FTIR spectroscopy measurements probing at 487 nm are not possible. Measurements on "dilute" samples are still possible, however. The term "dilute samples" refers to samples prepared under 'more-standard' conditions, in a 10 × 5 mm cuvette, with concentration adjusted to achieve an optical density of ~1.6 at the peak of the Q_y band at ~679 nm.

3 . Results

Below we will be considering *menB*$^-$ PSI particles that have been incubated in the presence of either PhQ or 2MNQ. It will be shown that PhQ or 2MNQ is incorporated into the A_1 binding site in these PSI particles. We will refer to these *menB*$^-$ PSI particles simply as PSI with PhQ or 2MNQ incorporated. We will also refer to regular *menB*$^-$ PSI particles as PSI with PQ_9 incorporated.

PSI samples with "low" Q_y peak absorption (1.6 or less) we will call dilute samples, to distinguish them from the samples we use in FTIR measurements, which we will call "concentrated" samples. Concentrated samples can be probed at 703 and 800 nm, but not at 487 nm. Concentrated samples can also be studied spectroscopically at 77 K without cryoprotectant, while dilute samples cannot.

3.1. Nanosecond time-resolved visible absorption spectroscopy

Fig. 2 shows RT flash-induced absorption changes at 703 and 800 nm for PSI with PQ_9, 2MNQ and PhQ incorporated, on a 350 ns timescale. Data are shown for concentrated (*left*) and dilute (*right*) samples. Also shown are data obtained using WT cyanobacterial PSI particles from *S6803* (with PhQ naturally present in the A_1 binding site). The "spike" observed in the first ~10 ns following laser excitation is an artifact due to imperfect subtraction of changes related to scattering and possibly fluorescence from the sample (Data associated with scattering from the sample was collected using the laser to excite samples but without probing light. This data was subtracted from the experimental data but, clearly, such a subtraction is imperfect). This "spike" should have a temporal width close to the instrument response, and is an artifact that in no way impacts any of the conclusions in this manuscript.

For the data in Fig. 2, several points are noteworthy: 1) The ns kinetics are similar for both concentrated and dilute samples. 2) The flash-induced absorption changes are identical for WT PSI from *S6803* and for *menB*$^-$ PSI with PhQ or 2MNQ incorporated. 3) The ns decay phases observed for PSI with PQ_9 incorporated are not observed for the other PSI samples.

Probe wavelengths at 703 and 800 nm are used primarily to monitor absorption changes associated with P700 and $P700^+$, respectively [29]. Since the P700 ground state recovers in tens of milliseconds, via $P700^+F_{A/B}^-$ charge recombination [25,30,31], no kinetic evolution of the absorption changes associated with P700 and $P700^+$ is expected in a 350 ns time range. This is essentially the case for WT PSI, and *menB*$^-$ PSI with PhQ or 2MNQ incorporated, where the kinetic traces are essentially flat over the 350 ns timescale. For PSI with PQ_9 incorporated, however, the absorption changes evolve considerably over the 350 ns timescale.

For PSI with PQ_9 incorporated the data at 703 nm is adequately described by a single exponential function with time constant of 96–103 ns. If the data at 800 nm is fitted to a single exponential function, a lifetime of 57–70 ns is calculated. From an evaluation of the residuals associated with this fit, it is clear that a single exponential function does not adequately describe the data. If the data at 800 nm is fitted to a bi-exponential function, lifetimes of 33 and 107 ns (Fig. 2A) or 23 and 105 ns (Fig. 2B) are calculated.

For PSI with PQ_9 incorporated the initial ($t = 0$), positive, flash-induced absorption change at 800 nm is greater than it is for PSI with PhQ incorporated. As a result of the ns kinetic phases, however, the positive absorption change at $t = 350$ ns, is smaller for PSI with PQ_9 incorporated compared to PSI with PhQ incorporated. On the other hand, for PSI with PQ_9 incorporated, the initial ($t = 0$), negative, flash-induced absorption change at 703 nm is *smaller* than it is for PSI with PhQ incorporated, and as a result of the ns kinetic phases, this difference becomes larger.

The ~23–107 ns decay phases in PSI with PQ_9 incorporated have not been observed before, and their origin is uncertain. In addition to these nanosecond decay phases, microsecond decay phases are also observed in PQ_9-incorporated PSI (data not shown). Since decay phases are observed at both 800 and 703 nm, wavelengths that are normally associated with $P700^+$ and P700, respectively, we tentatively suggest that these nanosecond decay phases could be due to ^{3}P700 formation, and the microsecond phase due to the decay of ^{3}P700. When ET from A_0^- to A_1 is blocked, the formation and decay of ^{3}P700 state are known to occur on ns and μs timescales, respectively [32]. While the features of the kinetics obtained at 800 nm for PSI with PQ_9 incorporated (Fig. 2A, B; blue) are comparable to the absorption change measured at 820 nm on PSI RC devoid of A_1, F_X, and $F_{A/B}$ [33], it is not clear if the extinction

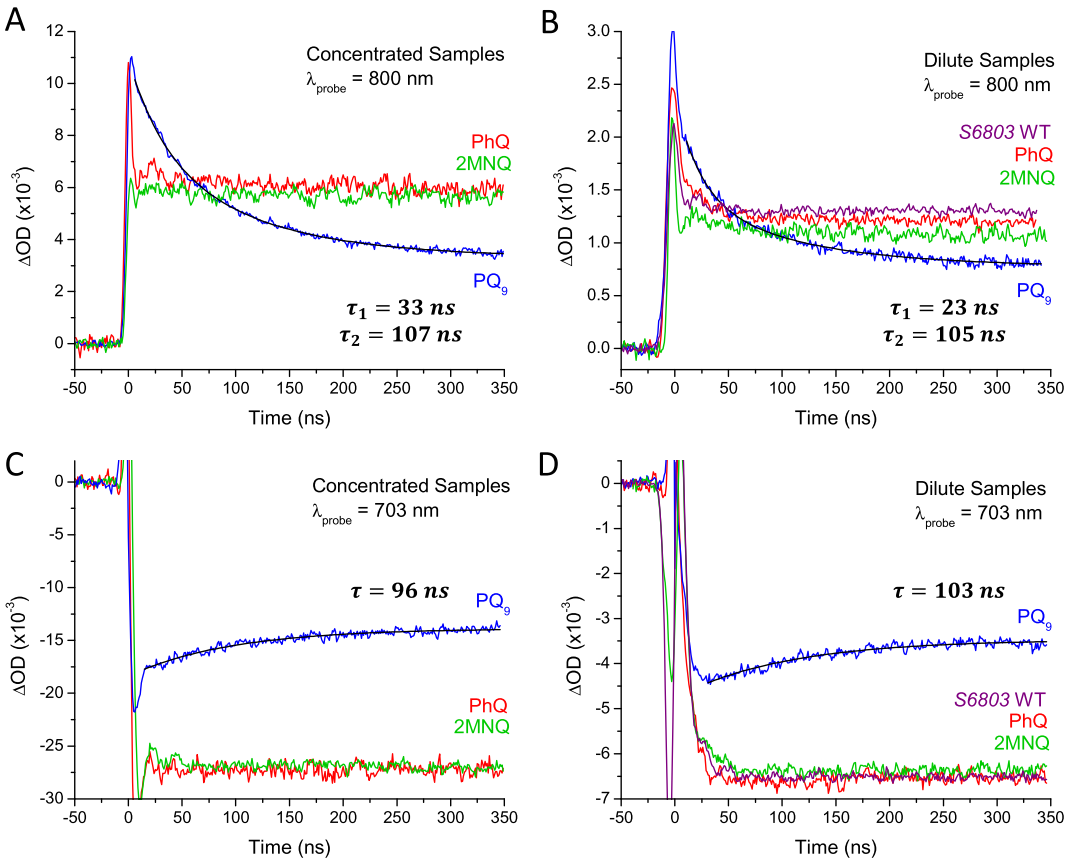

Fig. 2. RT flash-induced absorption changes at 800 (A, B) and 703 (C, D) nm on a 350 ns timescale for *menB*$^-$ PSI with PQ_9 (*blue*), 2MNQ (*green*), and PhQ (*red*) incorporated. Data for both dilute (B, D) and concentrated (A, C) PSI samples are shown. At 800 nm, for PSI with PQ_9 incorporated (*blue*), the data is best fit to two exponentials with lifetimes of 33 and 107 ns (A) or 23 and 105 ns (B). The fitted bi-exponential functions (*black*) are also shown in A and B. At 703 nm, the data is adequately fit to a single exponential with lifetime of 96 ns (C) or 103 ns (D). These fitted single exponential functions are also shown in C and D (*black*). Data is also shown for dilute WT PSI particles from *S6803* (*magenta*) (B, D).

coefficients of P700 and ^{3}P700 at 703 nm could give rise to the observed absorption changes at 703 nm.

Time-resolved visible spectroscopy on *menD1*$^-$ PSI from *Chlamydomonas reinhardtii* also exhibit ~30 ns and tens of microseconds decay phases when ET beyond A_0^- is blocked (because plastoquinol is present in the A_1 binding site) [34,35]. These observed ns and μs decay phases were probed at both 320 nm and 430 nm, and were assigned to $P700^+A_0^-$ radical pair recombination leading to ^{3}P700 formation and then its subsequent decay [34,35].

A more detailed study of the ns and μs decay phases observed in PSI particles with PQ_9 incorporated will be presented elsewhere. However, since the replacement of PQ_9 with other quinones is correlated to the disappearance of these ns and μs decay phases (Fig. 2), we often use the differences in the kinetics between PSI with PQ_9 incorporated, and the other PSI samples to assess the extent of quinone incorporation into the A_1 binding site.

In Fig. 2 the data for the dilute PSI samples are scaled to a sample absorbance at ~680 nm (Q_y peak) of 1.6. Fig. 2 indicates that the concentrated PSI samples lead to absorption changes that are nearly six times greater than that found for dilute PSI samples. The kinetics are the same for both concentrated and dilute samples, however. In addition the ratio of the amplitudes of the absorption changes for both concentrated and the dilute samples are the same. That is:

$$\frac{\Delta A_{800}^{t=0}(\mathrm{PhQ})}{\Delta A_{800}^{t=0}(\mathrm{PQ_9})} \sim 0.7,\ \frac{\Delta A_{800}^{t=350\mathrm{ns}}(\mathrm{PhQ})}{\Delta A_{800}^{t=350\mathrm{ns}}(\mathrm{PQ_9})} \sim 1.6,\ \frac{\Delta A_{703}^{t=0}(\mathrm{PhQ})}{\Delta A_{703}^{t=0}(\mathrm{PQ_9})} \sim 1.6,\ \text{and}\ \frac{\Delta A_{703}^{t=350\mathrm{ns}}(\mathrm{PhQ})}{\Delta A_{703}^{t=350\mathrm{ns}}(\mathrm{PQ_9})} \sim 1.8,$$

where an expression of the form $\Delta A_{800}^{t=0}(\mathrm{PhQ})$ represents the initial ($t = 0$) flash-induced absorption change at 800 nm for PSI with PhQ incorporated.

From the data in Fig. 2 at RT (as well as the data discussed below), since we see the same kinetics with the same amplitude ratios for both dilute and concentrated samples, we conclude that there are no concentration dependent artifacts to consider, and that conclusions drawn from work on concentrated samples are equally applicable to dilute samples.

3.2. Room temperature $P700^+F_{A/B}^-$ radical pair recombination

$P700^+F_{A/B}^-$ charge recombination is most easily probed at ~703 nm on a millisecond (ms) timescale [29]. At RT, for WT PSI (or *menB*$^-$ PSI with PhQ incorporated), radical pair recombination is characterized by a time constant of ~80 ms (see [30] and references therein). Fig. 3 shows RT flash-induced absorption changes on millisecond timescales for dilute PSI samples with (A) PQ_9 and (B) 2MNQ incorporated. The data in each are fitted to a single exponential function (plus a constant). The fitted decays are also shown in Fig. 3A and B, and are characterized by time constants of 3.2 and 14.4 ms, respectively. A decay constant of 3.2 ms is the same as that found previously for *menB*$^-$ PSI with PQ_9 incorporated [25,36]. For PSI with 2MNQ incorporated, a $P700^+F_{A/B}^-$ lifetime of ~14 ms has not been reported (although see [37]). The fact that millisecond decay phases are observed indicates that the A_1 binding site is occupied. The fact that the time constants observed are very different to that found for WT PSI, or for *menB*$^-$ PSI with PhQ incorporated, indicates that PQ_9 or 2MNQ is present in the A_1 binding site.

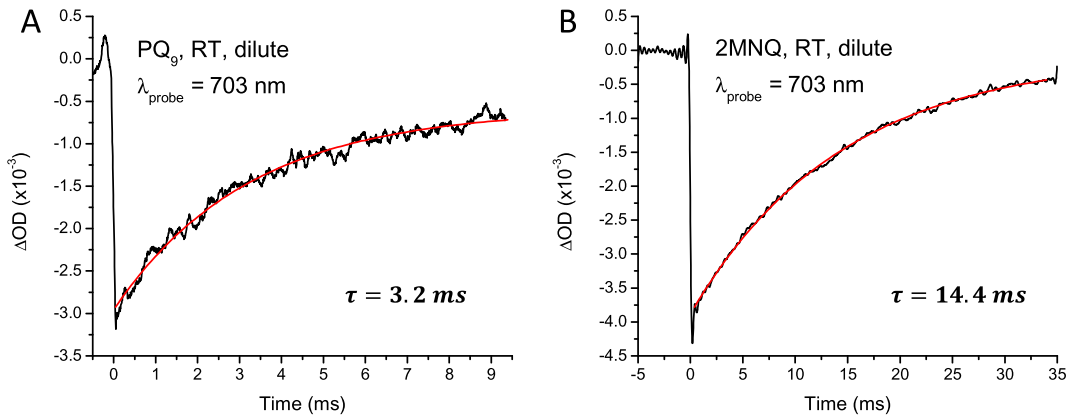

Fig. 3. RT flash-induced absorption changes at 703 nm on 10–35 ms timescales for *menB*$^-$ PSI samples with (A) PQ_9 and (B) 2MNQ incorporated into A_1 binding site. Measurements are shown for dilute samples but similar results are found for concentrated samples (not shown). The data in both figures were fitted to a single exponential function (plus a constant). The fitted functions are shown (*red*) along with the calculated time constants.

For PSI with PQ_9/2MNQ incorporated ~23/12% of the absorption change at 703 nm (Fig. 3) does not decay on the timescale considered. This is reminiscent of that found in WT PSI particles, where it is found that ~10% of the initial absorption change does not decay with a characteristic ~80 ms time constant. These longer lived components are presumably associated with ET from the terminal iron sulfur clusters to an external acceptor, such as oxygen [30].

3.3. $P700^+A_1^-$ to $P700^+F_x^-$ forward electron transfer at room temperature

Forward ET from A_1^- to F_X in PSI is most easily monitored at ~487 nm [9,38]. Fig. 4 shows flash-induced absorption changes at 487 nm for (dilute) *menB*$^-$ PSI with (A) PhQ, (B) PQ_9 and (D) 2MNQ incorporated. Fig. 4B shows absorption changes at 487 nm for (dilute) WT PSI samples. Different timescales were covered for each sample so that the dominant decay phase can be easily visualized.

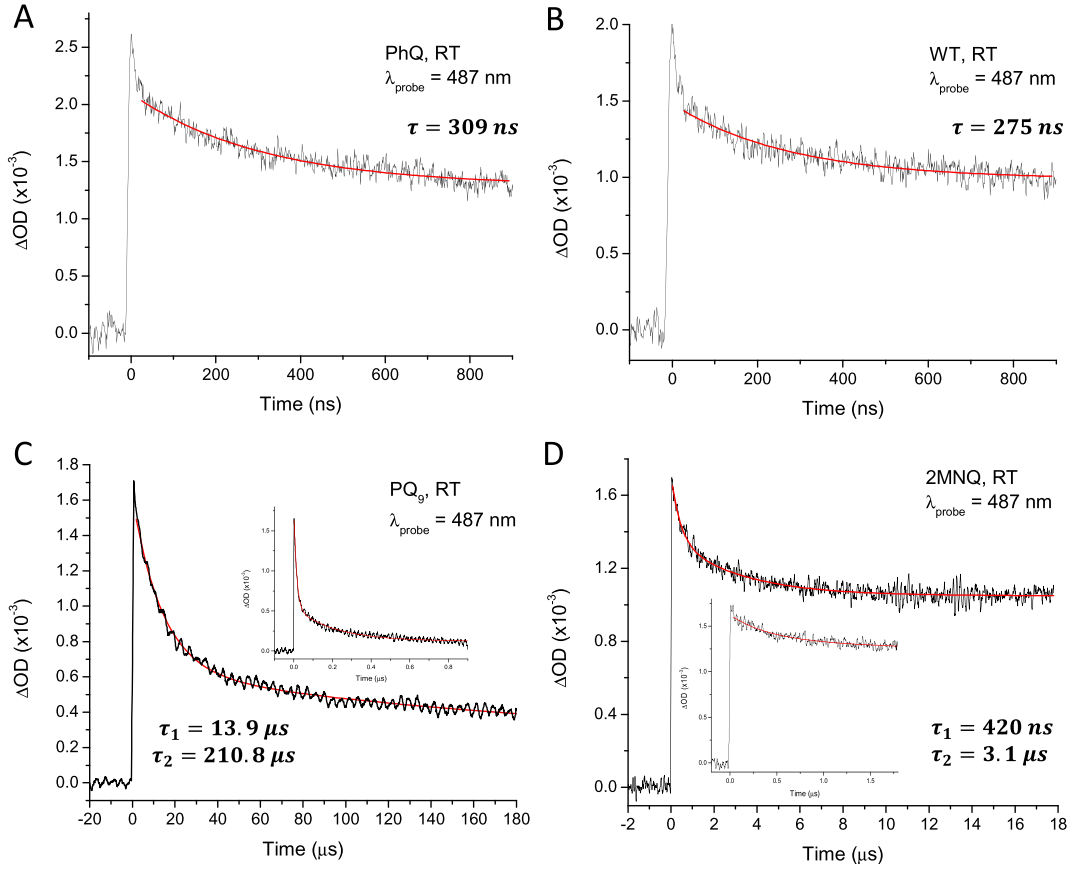

Fig. 4. Room temperature flash-induced absorption changes at 487 nm for *menB*$^-$ PSI samples with (A) PhQ, (C) PQ_9 and (D) 2MNQ incorporated into A_1 binding site. For comparison, measurements for WT PSI particles from *S6803* are also shown (B). Measurements are for dilute samples only as the absorbance at 487 nm for concentrated samples prohibits spectroscopic measurement. The calculated fitted functions (*red*) and time constants are also shown. Inset in C and D shows absorption changes over shorter 0.9 and 1.8 μs time windows, respectively.

For PSI with PhQ incorporated, a decay phase with time constant of ~20 ns is observed (Fig. 4A, B). The amplitude of this decay phase cannot be reliably estimated given the available time resolution. There is little doubt, however, that it is at least partially associated with B branch ET, which is known to occur on such a time scale [9].

Excluding the data in the first ~30 ns following the laser flash, and by fitting the data in Fig. 4A and B to a single exponential function, a time constant of 275–309 ns is calculated. For PSI from *S6803* at RT, a time constant of 340 ns has been found previously [9], in relatively good agreement with the data presented here. The data in Fig. 4A and B have been scaled, so the signal at 487 nm is slightly larger for *menB*$^-$ PSI with PhQ incorporated, compared to WT.

For regular *menB*$^-$ PSI with PQ_9 incorporated the kinetics are clearly bi-exponential (Fig. 4C). Fitting the data in Fig. 4C to a bi-exponential function, time constants of 13.9 and 210.8 μs are calculated. Previously, for *menB*$^-$ PSI with PQ_9 incorporated, two phases of forward ET from A_1^- to F_X have been found with lifetimes of 11.4–18.1 and 306–377 μs [25], in good agreement with our observations. These fast and slow phases have tentatively been assigned to $A_{1B}^- \rightarrow F_X$ and $A_{1A}^- \rightarrow F_X$ ET, respectively [16].

The RT flash-induced absorption changes at 487 nm for dilute *menB*$^-$ PSI with 2MNQ incorporated, on an 18 μs timescale, are shown in Fig. 4D. In addition to a microsecond decay phase, Fig. 4D indicates that faster, nanosecond phases also contribute to the absorption change. To better resolve these components measurements were made on a 1.8 μs timescale (*inset*). By fitting the data to a bi-exponential function, time constants of 420 ns and 3.1 μs are found. The rates of forward ET from A_1^- to F_X with 2MNQ occupying the A_1 binding sites have not been reported previously. However, following on from the suggested origin of the fast and slow phases for PSI with PQ_9 incorporated, we tentatively suggest that the fast and slow phases observed at 487 nm for PSI with 2MNQ incorporated are due to A_{1B}^- to F_X and A_{1A}^- to F_X ET, respectively.

3.4. $P700^+A_1^-$ charge recombination at 77 K

Flash-induced absorption changes at 703 and 800 nm at 77 K were measured using only concentrated PSI samples. Fig. 5 shows flash-induced absorption changes at 800 and 703 nm at 77 K for concentrated PSI with PQ_9 (A, B), PhQ (C, D) and 2MNQ (E, F) incorporated, on a 1 ms timescale. For PSI with PQ_9/PhQ/2MNQ incorporated into the A_1 binding site, the data at 703 and 800 nm was fitted simultaneously to a single exponential function, and a 250/338/240 μs time constant was calculated, respectively.

From previous TR step-scan FTIR DS studies on *menB*$^-$ PSI samples at 77 K (with PQ_9 incorporated), it has been shown that $^3P700$ is formed in a fraction of the PSI particles, presumably because in this fraction PQ_9 is not functional, or perhaps not even present [39]. At 77 K, the decay of $^3P700$ and radical pair recombination are characterized by similar time constants. Thus it is not possible to distinguish between the two processes at 77 K on the basis of time constants. For this reason we will not consider the data obtained at 77 K for PSI with PQ_9 incorporated, and we will focus only on data obtained at 77 K for PSI with PhQ or 2MNQ incorporated.

3.5. Time-resolved step-scan FTIR difference spectroscopy at 77 K

Fig. 6 shows absorption changes at four IR frequencies, obtained using concentrated PSI particles with PhQ or 2MNQ incorporated at 77 K. The four kinetic traces were fitted simultaneously to a single decaying exponential component plus a constant (non-decaying) component. The fitted functions are shown, and are characterized by a time constant of 301/241 μs for PSI with PhQ/2MNQ incorporated, respectively. The absorption changes at 1754 cm^{-1} contain contributions that are associated with the decay of $P700^+$ and A_1^-, while the changes at 1748 cm^{-1} contain contributions that are associated with the recovery of P700 and A_1 [40]. The absorption changes at 1495 and 1415 cm^{-1}

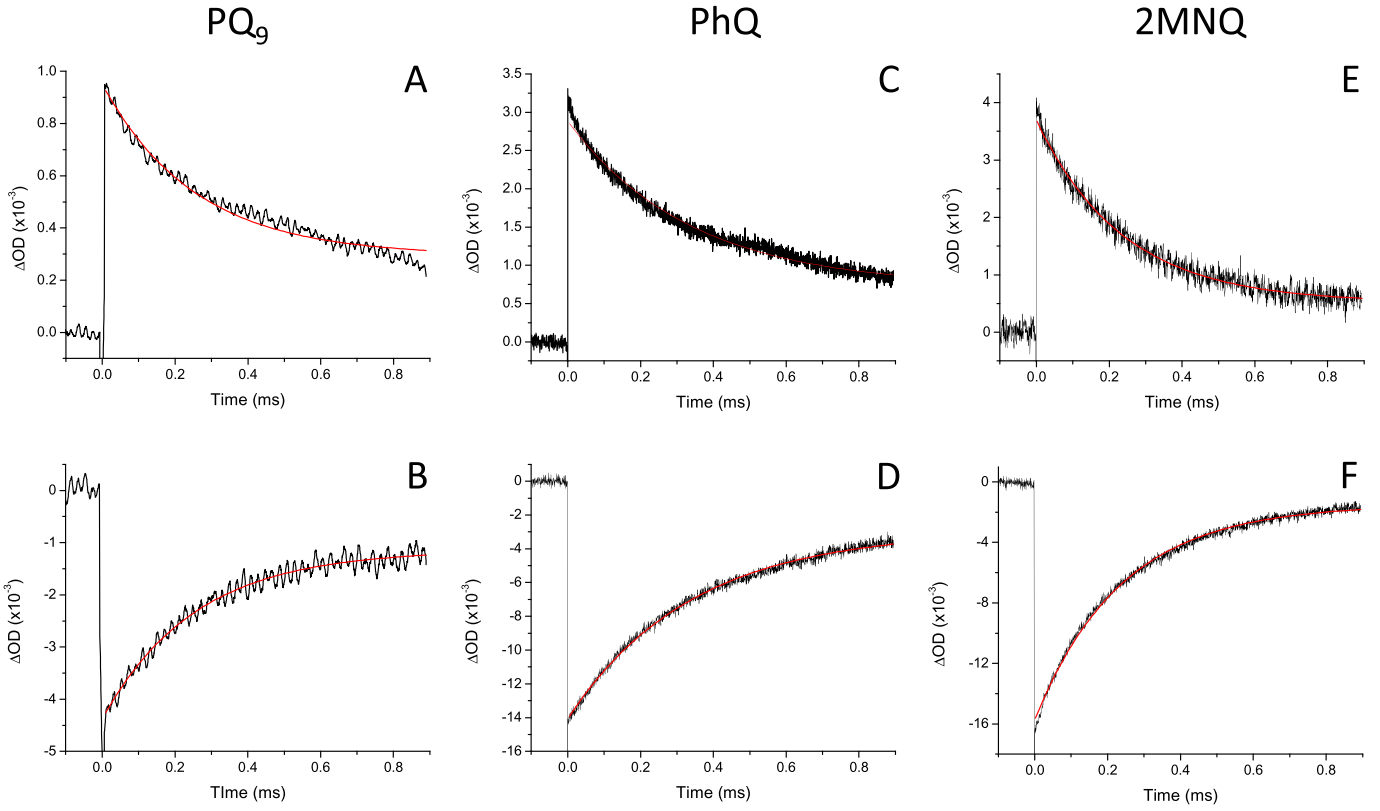

Fig. 5. Low temperature (77 K) flash-induced absorption changes at 800 (A, C, E) and 703 nm (B, D, F) for concentrated PSI samples with PQ_9 (A, B), PhQ (C, D) and 2MNQ (E, F) incorporated. The data at both probe wavelengths were fitted simultaneously to a single exponential function (*red*) and a lifetime of 250/338/240 μs was calculated, respectively.

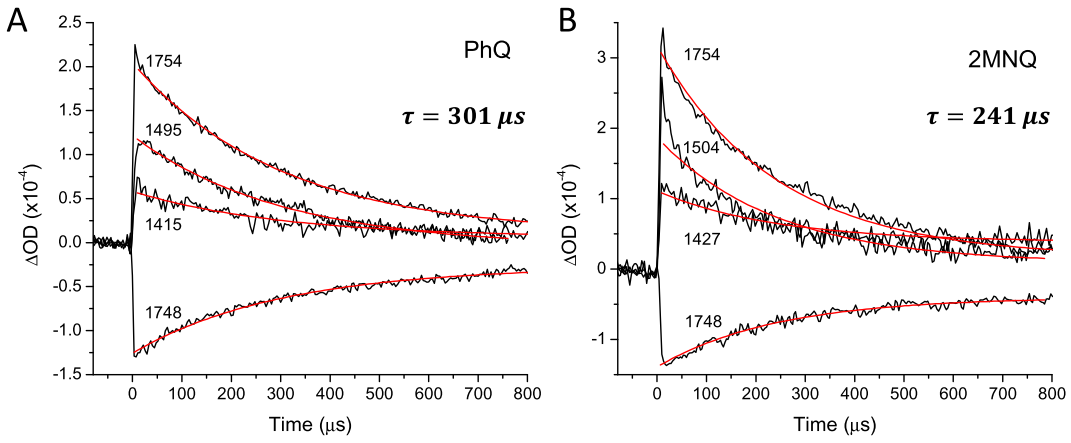

Fig. 6. Low temperature (77 K) flash-induced absorption changes at several IR frequencies obtained using PSI with (A) PhQ and (B) 2MNQ incorporated into the A_1 binding site. Data were collected in 5 μs increments. The four kinetics in each caption were fitted simultaneously to a single exponential plus a constant. The fitted functions are shown (red) and are characterized by a time constant of 301 and 241 μs, respectively.

in Fig. 6A are mostly due to the decay of PhQ^- in the A_1 binding site [40]. The absorption changes at 1504 and 1427 cm^{-1} in Fig. 6B are mostly due to the decay of $2MNQ^-$ in the A_1 binding site [41].

For PSI with PQ_9 incorporated, absorption changes at several IR frequencies have been presented previously, and a time constant of 208 μs was found [39]. However, this 208 μs decay phase, which accounts for >80% of the signal amplitude at 1594 cm^{-1}, is due to the decay of $^3P700$ and not $P700^+A_1^-$ [39].

Fig. 6 demonstrates that radical pair recombination at 77 K is faster for PSI with 2MNQ incorporated than for PSI with PhQ incorporated (241 *vs.* 301 μs). Such a result also follows from Fig. 5, where radical pair recombination at 77 K is characterized by a time constant of 240/338 μs for PSI with 2MNQ/PhQ incorporated, respectively. Thus the low temperature (77 K) TR visible and IR data are in good agreement. This comparison is a strong indication of the validity and applicability of the TR step-scan FTIR DS approach for the studies of quinones in the A_1 binding site in PSI at 77 K.

Table 1
Summary of time constants calculated for PSI particles with different quinones incorporated. At 77 K only concentrated samples were studied. The ratio of the initial amplitudes at 77 K and RT (column 5) indicates the percentage of PSI particles in which reversible ET processes are occurring at 77 K. The ratio of the monoexponential decay amplitude at 77 K to the initial amplitude at RT is listed also (column 6). This latter ratio gives a measure of the percentage of PSI particles in which $P700^+A_1^-$ charge recombination occurs at 77 K. At 298 K, for PSI with PQ_9 incorporated, the signal amplitudes after the ~30–100 ns decay phases are used.

Sample	Temp. (K)	λ_{pr} (nm)	Lifetime/amplitude (%)	$\Delta A_{77K}/\Delta A_{RT}$ (%)	$\Delta A_{77K}^{decay}/\Delta A_{RT}$ (%)
PQ_9	298	703	3.2 ms/79.9		
	298	487	13.9 μs/65.2		
			210.8 μs/25.2		
	77	703	250 μs/73.9	30.0	21.1
	77	800	250 μs/69.1	25.7	16.7
	77	IR	208 μs [39]		
PhQ	298	703	>80 ms [30]		
	298	487	~15 ns [9]		
			309 ns/30.9		
	77	703	338 μs/79.1	51.8	36.9
	77	800	338 μs/75.0	49.3	39.0
	77	IR	301 μs		
2MNQ	298	703	14.4 ms/98.0		
	298	487	420 ns/20.2		
			3.1 μs/19.0		
	77	703	240 μs/90.6	60.8	57.4
	77	800	240 μs/86.1	66.3	58.3
	77	IR	241 μs		

The time constants and associated decay amplitudes discussed in this manuscript for the various PSI particles, at 298 and 77 K, are summarized in Table 1.

4. Discussion

4.1. Indicator of quinone incorporation into the A_1 binding site in $menB^-$ PSI

All of the data presented here indicate the successful incorporation of foreign quinones into the A_1 binding site of *menB*$^-$ PSI. The RT forward ET (A_1^- to F_X) and charge recombination ($P700^+F_{A/B}^-$) rates probed at 487 nm and 703 nm respectively, for PSI with PQ_9 and PhQ incorporated, agree well with previously reported values. In PSI with 2MNQ incorporated, the forward ET (Fig. 4) and charge recombination rates (Fig. 3) are highly distinguishable from those for PSI with PQ_9 or PhQ incorporated. The amplitudes of the decay phases suggest a very high level of 2MNQ incorporation into the A_1 binding site.

The ns kinetics probed at 800 or 703 nm (Fig. 2) also serve as a useful indicator of successful quinone incorporation, since PSI with PQ_9 in the A_1 binding site exhibits ~30–100 ns decay phases that are not observed using PSI with PhQ or 2MNQ incorporated. Since the ns decay phases disappear when PhQ or 2MNQ is incorporated into the A_1 binding site, these ns phases probably relate to a lack of functionality of the A_1 binding site in a portion of the PSI particles, either because the A_1 binding sites are unoccupied, or because the A_1 binding sites are occupied by non-functional species, such as plastoquinol (PQH_2). In either case, ET to A_1 is blocked and $P700^+A_0^-$ could recombine to yield $^3P700$. Previous TR FTIR DS studies do indicate that $^3P700$ is formed in a fraction of PSI samples with PQ_9 incorporated at 77 K, but it is unclear if it is this fraction of PSI particles that give rise to the ns decay phases at RT. As mentioned above, it is unclear if a difference in the extinction coefficients between $P700^+$ and $^3P700$ could explain the absorption changes at 800 and 703 nm. Therefore, the origin of the ~30–100 ns decay phases observed at RT for PSI with PQ_9 incorporated remains an open question that will be addressed in future publications. The main point for the present manuscript is that the loss of ~30–100 ns decay phases for *menB*$^-$ PSI incubated in the presence of other quinones is an indicator that the new quinone has been incorporated into the A_1 binding site.

4.2. Redox potential of quinones in the A_1 binding site

Observed rates of forward ET can be used to estimate the redox potential of the quinone in the A_1 binding site, and Eq. (1) outlines an

empirical approximation relating the rate of intra-protein ET (k) to the edge-to-edge distance between the electron carriers (R), the standard reaction free energy (ΔG^0), and the reorganization energy (λ) [42]. In Eq. (1) k is measured in s^{-1}; R in Å; ΔG^0 and λ in eV.

$$\log k = 13-(1.2-0.8\rho)\cdot(R-3.6)-\gamma\left(\Delta G^0+\lambda\right)^2/\lambda \quad (1)$$

The parameter ρ gives a measure of the protein packing density, a value that is correlated to the tunneling barrier of the medium. A mean value of 0.76 is obtained in a survey of packing densities in a series of ET systems [43], and this number is used here. In the classical treatment of Marcus, γ is given by $F/(4\times 2.303 k_BT)$ [44,45]. In the quantum mechanical treatment recommended by Moser and Dutton, γ is modified by the Hopfield approximation that replaces k_BT with $\hbar\omega/2$ coth $[\hbar\omega/2k_BT]$ [44,46,47]. With $\hbar\omega = 0.056$ eV and T = 298 K, γ is calculated to be 3.1. Substituting the values for ρ and γ into Eq. (1) results in Eq. (2). Eq. (2) indicates that a change in ET rate may reflect a change in R, ΔG^0 and/or λ.

$$\log k = 15-0.6R-3.1\left(\Delta G^0+\lambda\right)^2/\lambda \quad (2)$$

Previous EPR studies have shown that the distances from P700 to PQ_9, 2MNQ, or PhQ in the different PSI particles are nearly identical [24,48]. The reorganization energy associated with ET from A_1^- to F_X is also commonly assumed to be unaffected by the type of quinone in the A_1 binding site. Therefore, a change in the rate of ET from A_1^- to F_X is generally considered to be associated with a change in the Gibbs standard reaction free energy.

The average edge-to-edge distance (established using the 2.5 Å PSI crystal structure) between the quinone in the A_1 binding site and F_X is ~9.0 Å [17,49]. However, distances in the 6.8–11.3 Å range have also been used [18,25,49,50]. This wide range of edge-to-edge distances will be considered in calculations presented below. Commonly used reorganization energies typically fall in the 0.7–1.0 eV range [18,25,50], and values in this range will also be considered in calculations presented below.

Earlier estimates of the midpoint potential of PhQ in the A_1 binding site were undertaken assuming unidirectional ET, and a single midpoint potential is assigned to PhQ in both the A_{1A} and A_{1B} binding sites. As experimental support for bi-directional ET emerged, differences in A_{1A} and A_{1B} midpoint potentials between 25–173 meV have been proposed to account for differences in A and B branch ET rates [17,18]. Furthermore, simulations suggested that the $A_{1A}^- \rightarrow F_X$ ET process is slightly endergonic, while the $A_{1B}^- \rightarrow F_X$ process is slightly exergonic [17,49].

Table 2
Calculated Gibbs standard reaction free energy (in meV) for A_1^- to F_X ET in PSI, with PhQ, 2MNQ, and PQ_9 in the A_1 binding site.

R (Å)	λ (eV)	ΔG^0 (meV)					
		PhQ		2MNQ		PQ_9	
		$\tau = 15$ ns	$\tau = 309$ ns	$\tau = 420$ ns	$\tau = 3.1$ µs	$\tau = 13.9$ µs	$\tau = 211$ µs
6.8	0.7	136	298	313	405	470	579
	0.8	94	267	283	382	451	567
	1.0	−0.6	193	211	321	399	529
8	0.7	32	213	229	329	399	514
	0.8	−34	176	193	300	375	498
	1.0	−125	91	111	230	313	451
9	0.7	−67	135	153	261	335	457
	0.8	−123	93	112	228	307	436
	1.0	−243	−1.4	20	149	237	382
11.3	0.7	−401	−79	−55	82	172	313
	0.8	−480	−136	−110	36	132	283
	1.0	−643	−257	−229	−65	42	211

Forward ET from PhQ^- to F_X on the A branch is characterized by a time constant of 309 ns (Fig. 4A and Table 2). Using this time constant in Eq. (2), along with $R = 9.0$ Å and $\lambda = 0.7$ eV, ΔG^0 is calculated to be +135 meV. ET from A_{1B}^- to F_X is reported to be in the 10–25 ns range [9–12]. Using these time constants, along with $R = 9.0$ Å and $\lambda = 0.7$ eV in Eq. (2) yields ΔG^0 values in the −98 to −28 meV range. Thus the midpoint potential of A_{1A} is calculated to be 163–233 mV more positive than A_{1B}. The lower end of this difference in free energy between A_{1A} and A_{1B} is in agreement with the range computed by Ishikita and Knapp (155–166 mV), and with that calculated by Ptushenko et al. (173 mV) [18,51].

For PSI with PQ_9 incorporated, previously reported values of the Gibbs standard reaction free energy for the $A_1^- \rightarrow F_X$ ET process are +12, +35, and +95 meV [25,36]. However, with the time constant of 13.9 µs measured here (Fig. 4, Table 2), along with $R = 9.0$ Å and $\lambda = 0.7$ eV, ΔG^0 is calculated to be +335 meV using Eq. (2). If the observed 211 µs time constant is taken as the rate of forward ET in the second branch, then ΔG^0 is calculated to be +456 meV, and there is a 121 meV difference in ΔG^0 between the quinones on each branch.

Similarly, for PSI with 2MNQ incorporated, with forward ET being characterized by time constants of 420 ns and 3.1 µs, ΔG^0 is calculated to be +154 meV and +261 meV, respectively. The calculated difference in ΔG^0 between 2MNQ on the A and B branches is therefore 107 meV.

For all three quinones incorporated, a difference in midpoint potentials of A_{1A} and A_{1B} is calculated to be in the 100–200 mV range.

As indicated above, a wide range of parameters have been used in various applications of Marcus ET theory to PSI. Therefore, in addition to the parameters calculated above, values for ΔG^0 using other commonly reported parameters are listed in Table 2.

For PSI with PhQ incorporated, $\Delta G^0_{A1A/FX} = 135$ mV ($R = 9.0$ Å and $\lambda = 0.7$ eV) is calculated using the experimentally observed rate as input in Eq. (2). However, using this approach for PSI with 2MNQ and PQ_9 incorporated places the calculated $\Delta G^0_{A1A/FX}$ value at +261 and +457 mV (Table 2), both of which are unreasonably large (>$10k_BT$).

If the experimentally observed ET rates are used directly in Eq. (2) then this implies that the ET processes is virtually irreversible, requiring the forward ET rate to be much larger than the reverse ET rate. Another approach is to explicitly consider forward and reverse ET processes, in a so-called "quasi-equilibrium" model, that was initially proposed by Brettel et al., and later extended by Santabarbara et al. to include bi-directional ET [8,12,17,32,52]. In this quasi-equilibrium model, experimentally observed rates do not represent the intrinsic rate of ET that should be used in Eq. (2). Using this quasi-equilibrium modeling approach, Santabarbara et al. have suggested $\Delta G^0_{A1A/FX}$ and $\Delta G^0_{A1B/FX}$ values of +15 and −10 meV, respectively, for PSI with PhQ incorporated [17]. The very different values (compared to that listed in Table 2) are a reflection of the fact that the observed decay rates (Fig. 4) and intrinsic decay rates are quite different.

Fig. 7D shows the quasi-equilibrium model that we have used to simulate the experimental time-resolved data for PSI with PhQ, 2MNQ and PQ_9 incorporated. Simulation involves numerical solution of a series of first order, linear differential equations associated with the various radical pair state populations, with the various rate constants used as input (described in detail in [17]). Forward ET rates (shown in Fig. 7D) were computed using Eq. (2) with $R = 9.0$ Å and $\lambda = 0.7$ eV and appropriate values for ΔG^0. Reverse ET rates were calculated assuming a Boltzmann distribution ($T = 298$ K). In our model (Fig. 7D) the initial radical pair state populations ($[P700^+A_{1A}^-]$ and $[P700^+A_{1B}^-]$) were distributed evenly (50%/50%), although uneven distributions were found to yield similar results (not shown). In addition, the $F_X^- \rightarrow F_A$ ET rate was assumed to be unaffected by the type of quinone in the A_1 binding site.

For PSI with 2MNQ incorporated, $\Delta G^0_{A1A/FX}/\Delta G^0_{A1B/FX}$ was taken as +85/+60 meV, respectively (outlined in Fig. 7D). Substituting these values into Eq. (2) gave the rate constants in Fig. 7D, which were then used to calculate the temporal evolution of the $P700^+A_1^-$ population,

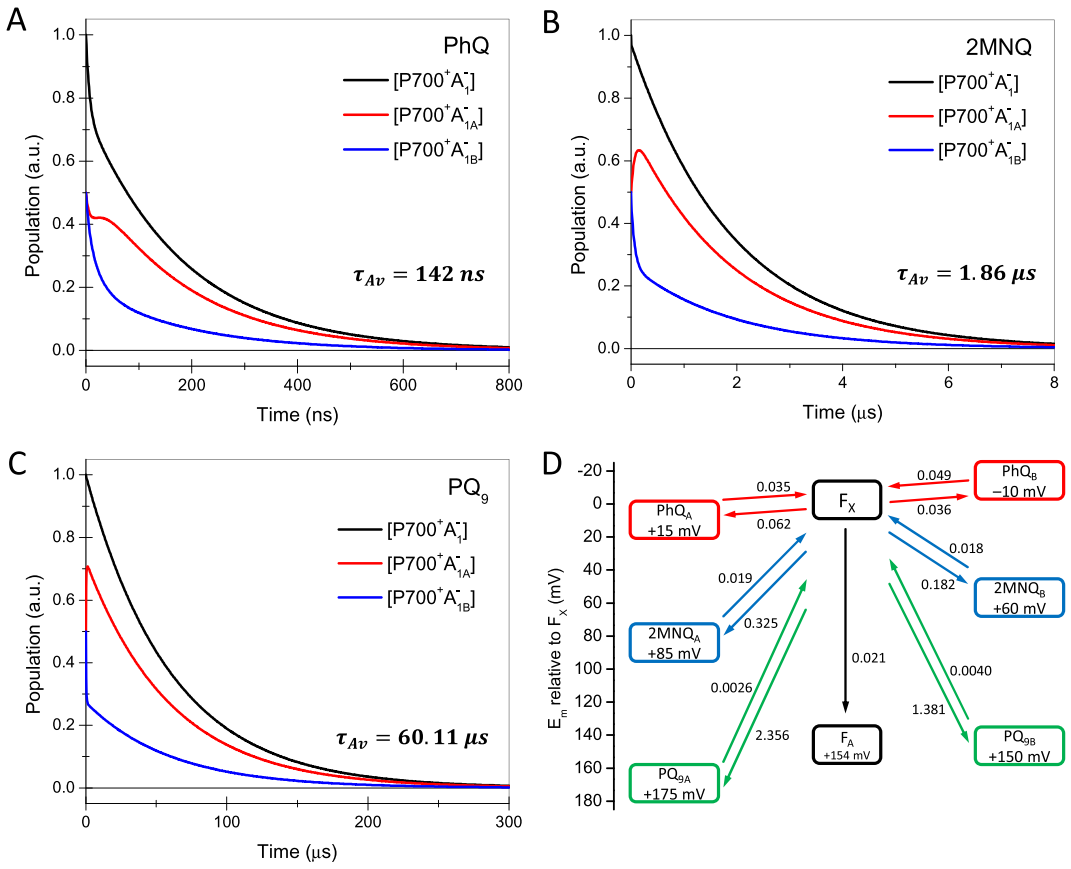

Fig. 7. Simulated temporal evolution of the population of radical pair states for PSI with (A) PhQ, (B) 2MNQ and (C) PQ_9 incorporated. Evolution of the $[P700^+A_{1A}^-]$ (*red*), and $[P700^+A_{1B}^-]$ (*blue*) populations are shown along with the sum of the two $[P700^+A_1^-]$ (*black*). (D) Kinetic model used in simulations. $\Delta G^0_{A1A/FX}/\Delta G^0_{A1B/FX}$ used are +15/−10, +85/+60 and +175/+150 meV for PSI with PhQ, 2MNQ and PQ_9 incorporated, respectively. Using these values in Eq. (2) (with R = 9.0 Å, λ = 0.7 eV, T = 298 K) the rate constants indicated in (D) are calculated (in units of ns^{-1}). The temporal profiles in A, B and C are a sum of several exponential components. The weighted average of the time constants (calculated as indicated in [17] for $[P700^+A_1^-]$ are 142 ns, 1.8 μs and 60 μs for PSI with PhQ, 2MNQ and PQ_9 incorporated, respectively.

which is shown in Fig. 7B. This solution is by no means unique, and represents merely a possible starting point for more refined analysis. The $P700^+A_1^-$ population evolution shown in Fig. 7B can be described by three time constants of 1.8 ns, 64.4 ns, and 1.92 μs, with associated decay amplitudes of 0.02, 0.01, and 0.97. By weighting the time constants by the appropriate amplitude and summing the results, an averaged time constant can be calculated [17]. For PSI with 2MNQ incorporated the averaged time constant is calculated to be 1.86 μs (Fig. 7B), which agrees well with the average time constant obtained experimentally (average of 420 ns and 3.1 μs components).

For PSI with PQ_9 incorporated, $\Delta G^0_{A1A/FX}/\Delta G^0_{A1B/FX}$ were taken as +175/+150 meV (Fig. 7D), and an average time constant of 60 μs is calculated. Taking the observed time constants of 14 μs and 211 μs (with amplitudes of ~0.7 and ~0.3), an average time constant of 73 μs is calculated, in good agreement with the simulation.

For PSI with PhQ incorporated, $\Delta G^0_{A1A/FX}/\Delta G^0_{A1B/FX}$ were taken as +15/−10 meV (Fig. 7D), and an average time constant is 142 ns is calculated, which is similar to that obtained previously using slightly different parameters and initial conditions [17].

In summary, the averaged time constant obtained using the quasi-equilibrium model for PSI with PhQ, 2MNQ or PQ_9 incorporated simulates well the overall trend in the lifetimes observed experimentally. Some specific details, such as the amplitude ratios associated with the fast and slow kinetic components observed experimentally is not well modeled. The modeling outlined here represents a starting point for more detailed modeling that will include further experimental work on PSI with several other different quinones incorporated into the A_1 binding site.

To obtain the quinone midpoint potential, E_m, from the calculated ΔG^0, the midpoint potential of F_X is required. A range of F_X midpoint potentials have been reported (−650 to −730 mV), however [16]. The calculated midpoint potential for PhQ in A_{1A} binding site, using the range of reported midpoint potentials for F_x, and ΔG^0 = +15 mV (R = 9.0 Å and λ = 0.7 eV) is −635 to −715 mV. Also by taking the values used in the quasi-equilibrium model, the ranges for the midpoint potential of 2MNQ and PQ_9 are 70 and 160 mV more oxidizing, respectively.

The midpoint potentials of PhQ, PQ_9 and 2MNQ in dimethylformamide (DMF) are −465 mV, −369 mV and −414 mV (*vs.* NHE), respectively [22,53]. These values place 2MNQ and PQ_9 51 and 96 mV more positive than PhQ, respectively.

According to an empirical formula derived by Iwaki et al., [53] the relationship between the midpoint potential in DMF ($E_{1/2}$) and that in the A_1 binding site of PSI (E_m) is:

$$E_m + 700\ \text{mV} = 0.69\left(E_{1/2} + 387\ \text{mV}\right) \quad (3)$$

Applying Eq. (3), the E_m of PQ_9, 2MNQ, and PhQ in the A_1 binding site is −682 mV, −718 mV, and −754 mV, respectively. This suggests that 2MNQ and PQ_9 are 36 and 72 mV more positive than PhQ *in situ*, respectively.

The differences in midpoint potentials calculated by directly using the experimental ET rates in Eq. (2) [for A_{1A}^-: +125 mV (2MNQ–PhQ); +324 mV (PQ_9–PhQ)] disagree considerably with the values associated with the quinone in DMF (+51 mV, +96 mV), or after correction using Eq. (3) (+36 mV, +72 mV). However, the differences in midpoint potentials calculated using the quasi-equilibrium model (+70 mV, +160 mV) are in good agreement with that estimated using Eq. (3).

These (positive) changes in midpoint potential on going from PhQ to PQ_9 or 2MNQ will result in the lowering the equilibrium constant between A_1 and F_X. Consequently, forward ET slows while recombination (between $P700^+$ and $F_{A/B}^-$) accelerates [36]. Such an effect is clearly observed in the data presented here, with recombination time constants going from ~80 ms (PhQ) to ~14 ms (2MNQ) and ~3 ms (PQ_9).

4.3. Heterogeneity in ET processes in PSI at 77 K

Forward ET from A_1^- to F_X is the predominant process in cyanobacterial PSI particles at RT. As the temperature is lowered ET in PSI becomes heterogeneous, with different fractions undergoing $P700^+A_1^-$ and $P700^+F_X^-$ charge recombination, while in a third fraction a virtually irreversible $P700^+F_{A/B}^-$ state is formed [8,54]. Unless F_X is pre-reduced, the $P700^+A_1^-$ recombination reaction at low temperature occurs only along the A branch [55]. The reasons underlying the changes in photochemistry as the temperature is lowered are not entirely clear. It has been proposed that the different fractions are due to the formation of frozen-in conformational substates that differ in free energy [32,55]. In support of this hypothesis, heterogeneous ET is observed to be correlated to the glass transition temperature of the medium (~180 K in 65% glycerol), at which the viscosity reaches 10^{13} poise [8].

The data presented here can be used to establish to what extent each of the above three processes ($P700^+A_1^-$, $P700^+F_X^-$, and $P700^+F_{A/B}^-$) contributes to PSI with the different quinones incorporated. Since we have used the same samples for measurement at 298 and 77 K, the amplitude of the flash-induced signals at the two temperatures can be directly compared. The initial ($t = 0$) absorption changes give a measure of PSI particles in which reversible ET reactions occur. At RT this fraction is assumed to be 100%. By comparing the initial amplitude of the flash-induced absorption changes at 298 and 77 K the fraction of PSI particles that undergo irreversible ET at 77 K can be estimated, assuming temperature independent extinction coefficients.

For PSI with PhQ incorporated at RT, the initial amplitude of the flash-induced absorption change at 800/703 nm is ~6.5/−28 mOD, respectively (Fig. 2B and D). At 77 K the initial amplitude is ~3.2/−14.5 mOD, respectively (Fig. 5C and D). Thus 49–52% of the PSI particles participate in reversible ET at 77 K (Table 1), or 48–51% undergo irreversible ET at 77 K. From the absorption changes at 77 K (Fig. 5C and D), about 20% of the PSI particles decay with a time constant considerably longer than the 338 μs (Table 1). This long lived component is due to $P700^+F_x^-$ recombination. So, $P700^+A_1^-$ radical pair recombination occurs in about 37–39% of PSI particles at 77 K, while $P700^+F_x^-$ occurs in about 10–15% of PSI particles at 77 K. In WT PSI particles from *S. elongatus* at 77 K, $P700^+A_1^-$/$P700^+F_x^-$ charge recombination was shown to occur in ~45/20% of the PSI particles at 77 K, respectively, with irreversible ET occurring in ~35% of the PSI particles [8]. These results are in good agreement with the data presented here for *menB*$^-$ PSI from *S6803* with PhQ reincorporated.

For PSI with 2MNQ incorporated, at 77 and 298 K, the initial amplitude of the flash-induced absorbance change at 800/703 nm is ~4/−16.5 mOD (Fig. 5E, F) and 6/−27 mOD (Fig. 2A, B), respectively. So ~61–66% of the RCs participate in radical pair recombination at 77 K (Table 1), or 34–39% undergo irreversible ET. For PSI with 2MNQ incorporated at 77 K, ~6% of the RCs decay with a time constant considerably longer than 240 μs. So $P700^+F_x^-$ recombination occurs in ~6% of the PSI particles with 2MNQ incorporated at 77 K.

For PSI with PQ_9 incorporated at RT, after the ~100 ns phase is complete, the amplitude at 800/703 nm is 3.5/−14 mOD (Fig. 2A, B). At 77 K, the initial amplitude decreased by 70–75% to 0.9/−4.2 mOD at 800/703 nm, respectively (Fig. 5A and B). Of these diminished amplitudes, ~65–70% was accounted by the 250 μs decay phase. However, TR FTIR DS of PSI with PQ_9 in the A_1 binding site reveals this ~200 μs phase to be due to the decay of $^3P700$. Consequently, the contributions of the three processes are undetermined for PSI with PQ_9 incorporated at 77 K.

In summary, for PSI with 2MNQ incorporated the proportion of RCs undergoing $P700^+A_1^-$ recombination is considerably higher than for PSI with PhQ incorporated (~58% *vs.* ~39%, Table 1), while the fraction of RCs undergoing $P700^+F_X^-$ recombination is smaller (~6% *vs.* ~15%). An explanation for this observation will be discussed below.

4.4. Quinone redox potential and low temperature ET heterogeneity

Extending the frozen conformational substate hypothesis to include bi-directional ET, it was initially suggested that a certain fraction of the RCs are frozen in a conformation that facilitates ET in either the A branch or B branch [16,17,56]. In this model, the thermodynamically downhill ET from A_{1B}^- to F_X would form the irreversible state, while thermodynamically uphill ET from A_{1A}^- to F_X would result in $P700^+A_{1A}^-$ recombination reaction. This model does not provide an explanation for the fraction of $P700^+F_X^-$ state formed in repetitive flash experiments, however. In an attempt to address this issue, a distribution of cofactor midpoint potentials has been considered [32,55]. In purple bacterial reaction centers cofactor energy levels have been estimated to have a Gaussian width of $2\sigma \approx 100$ meV [57]. In the case of PSI, where the free energy gaps between cofactors is similar to the width of possible distributions, such a spread in midpoint potentials could give rise to a set of substates that results in heterogeneous ET at low temperature [32,55].

In this model, the substates are no longer required to use the A or B branch exclusively. However, EPR data does appear to indicate that the $P700^+A_1^-$ state observed at low temperature is associated only with A_{1A} [22,55]. Given this EPR data we associate the 340/240 μs time constants (for PSI with PhQ/2MNQ incorporated at 77 K) to $P700^+A_{1A}^-$ recombination.

$P700^+A_{1A}^-$ recombination is clearly faster for PSI with 2MNQ incorporated compared to PSI with PhQ incorporated. Such an observation is difficult to explain given that the free energy gap between A_{1A} and P700 is calculated to be smaller for 2MNQ in the A_1 binding site compared to PhQ. An increase in rate when the free energy gap decreases can be explained, however, by considering the large free energy gap between A_{1A}^- and $P700^+$ (~−1.10 eV) [49]. If a reorganization energy of ~0.6 eV is assumed, and thus $\Delta G° > \lambda$, the recombination process would take place in the inverted region [58]. This idea has been suggested previously for PSI ET reactions at 77 K [49]. In the inverted region a decrease in free energy would result in an increased rate, as is observed here.

An increase in the $P700^+A_{1A}^-$ recombination rate as the free energy gap is lowered also follows from Eq. (1) appropriately adjusted so that it is applicable at 77 K ($R = 18.1$ Å, $\lambda = 0.6$ eV, $\rho = 0.88$, $\gamma = 3.9$). From the measured rates (240 and 340 μs) the free energy gap for PSI with PhQ incorporated is ~−1.20 eV, which is ~19 meV more negative than that found for PSI with 2MNQ incorporated. That is, a faster rate is observed for a system in which the free energy gap is smaller. However, a ~19 meV difference in free energy between PhQ and 2MNQ incorporated into PSI is more than a factor of three smaller than the difference estimated using the quasi-equilibrium model along with the forward ET rates at RT (70 meV). Alternatively, if the free energy difference between PhQ and 2MNQ in PSI is the same at RT and 77 K (~70 meV) then one would expect the time constant for $P^+A_1^-$ recombination to decrease from ~340 μs to ~104 μs for 2MNQ in the A_1 binding site.

Clearly, there are factors that lead to discrepancies when the Marcus ET theory is applied to PSI at RT and 77 K. For example, a ~20 meV difference in free energy between PhQ and 2MNQ in PSI could be explained by a small change (~0.2 A) in the edge-to-edge distance when 2MNQ is

substituted for PhQ. In the above calculation it was assumed that the edge-to-edge distance between the pigments is unaltered on going from PhQ to 2MNQ. This assumption is based on EPR data, but a distance change of ~0.2 A is below the accuracy achievable in the EPR measurement [22,24]. Thus such a small distance change cannot be ruled out based on a consideration of EPR data. Given such complications, it is difficult to establish simply on the basis of the weak changes in ET rate whether light induced ET reactions in PSI at 77 K do indeed occur in the inverted region.

Perhaps the discrepancy between room and low temperature calculations could be explained on the basis of a change in the distribution of midpoint potentials of conformational substates and their effect on the rate of $P700^+A_{1A}^-$ recombination. In a case where a substate is frozen in an energetic configuration that places the free energy gap of A_{1A}^- and F_X to be positive but A_{1B}^- and F_X to be negative, an indirect accumulation of A_{1A}^- by inter-quinone ET via F_X may take place [55]. In such a scenario, the observed kinetics (which monitors P700 and $P700^+$) does not simply represent the oxidation of directly populated A_{1A}^-, but includes contributions from the indirect accumulation of A_{1A}^- from A_{1B}^-. These additional phases of ET would be expected to decrease the overall rate of the $P700^+A_1^-$ charge recombination reaction. Thus, the underestimation of difference in midpoint potentials of A_{1A}^- may be the result of this additional contribution included in the observed rates. Again, a number of mechanisms can explain the weak increase in ET rate (on going from PhQ to 2MNQ in the A_1 binding site), making it difficult to establish whether $P700^+A_{1A}^-$ recombination at 77 K occurs in the inverted region.

At 77 K PSI photochemistry is heterogeneous. The variation in the degree of heterogeneity for PSI with the different quinones incorporated was discussed above: For PSI with PhQ incorporated, irreversible charge separation occurs in 50% of the particles. $P700^+A_1^-$ recombines in ~40% of the particles, and $P700^+F_X^-$ recombines in ~10% of the particles (Table 1). In contrast, for PSI with 2MNQ incorporated, irreversible charge separation occurs in ~35% of the particles, $P700^+A_1^-$ occurs in about 60% of the particles, and $P700^+F_X^-$ recombines in ~5% of the particles (Table 1). Although detailed modeling has yet to be undertaken, the observed changes in heterogeneity can qualitatively be understood given the changes in the redox potentials that occur in exchanging PhQ for 2MNQ. If substitution of PhQ by 2MNQ shifts the midpoint potential of A_1^- by approximately +70 mV, then the reduction of terminal electron acceptors become less favorable, which could then potentially lead to a decrease in the amount of irreversible ET, as is observed here. Furthermore, a decrease in the number of reaction centers displaying $P700^+F_X^-$ recombination when 2MNQ is incorporated may also be explained as ET from A_{1A}^- to F_X becomes less favorable and A_{1A}^- to $P700^+$ ET becomes more favorable. So the alterations in the degree to which the different ET processes contribute at 77 K for PSI with the different quinones incorporated can be qualitatively explained on the basis of the calculated redox potentials of the different quinones in the A_1 binding site.

5 . Conclusions

1. 2MNQ and PhQ can displace PQ_9 and be incorporated almost quantitatively into the A_1 binding site in *menB*$^-$ PSI.
2. 30–100 ns decay phases are observed in native *menB*$^-$ PSI particles, but not in PSI with 2MNQ or PhQ reintroduced into the A_1 binding site.
3. At either room temperature or 77 K, light induced ET processes are governed by identical kinetics in dilute and highly concentrated PSI samples.
4. Highly concentrated samples form a clear and transparent glass at both room and low temperatures in ultrathin sample cells of ~5 μm thickness. This allows spectroscopy to be undertaken at 77 K using PSI samples in the absence of cryoprotectant.
5. Identical low temperature kinetics are observed in both the visible and infrared spectroscopy experiments.
6. The observed kinetics of $A_1^- \rightarrow F_X$ ET allow an estimate of the redox potential of PhQ. 2MNQ, and PQ_9 in the A_1 binding site.
7. Observed alterations in the degree of heterogeneity of ET processes at 77 K for PSI with different quinones incorporated can be understood in terms of the differences in redox potential of the quinones incorporated.

Acknowledgement

This report was made possible by a NPRP award [NPRP 4-183-1-034] from the Qatar National Research Fund (a member of The Qatar Foundation). The statements made herein are solely the responsibility of the authors. NZ acknowledges support from a fellowship from the Molecular Basis of Disease program at Georgia State University.

References

[1] P. Jordan, P. Fromme, H.T. Witt, O. Klukas, W. Saenger, N. Krauss, Three-dimensional structure of cyanobacterial photosystem I at 2.5 Angstrom resolution, Nature 411 (2001) 909–917.
[2] B. Ke, The Primary Electron Acceptor A_0 of Photosystem I, in: Photosynthesis: Photobiochemistry and Photobiophysics, Kluwer Academic Publishers, Dordrecht ; Boston, 2001. 555–578.
[3] J.H. Golbeck, D. Bryant, Photosystem I, Current topics in bioenergetics, vol. 16, Academic Press, New York, 1991, pp. 83–175.
[4] B. Ke, The Iron–sulfur center FeS-X of photosystem I, the photosystem I core complex, and interaction of the FeS-X domain with FeS-A. FeS-B, Photosynthesis: Photobiochemistry and Photobiophysics, Kluwer Academic Publishers, Dordrecht ; Boston, 2001, pp. 527–554.
[5] B. Ke, P430: The spectral species representing the terminal electron acceptor in photosystem I, Photosynthesis: Photobiochemistry and Photobiophysics, Kluwer Academic Publishers, Dordrecht ; Boston, 2001, pp. 505–526.
[6] S. Savikhin, Ultrafast optical spectroscopy of Photosystem I, in: J. Golbeck (Ed.), Photosystem I The Light-Driven Plastocyanin: Ferredoxin Oxidoreductase, Springer, Dordrecht, 2006, pp. 155–175.
[7] G. Hastings, S. Hoshina, A.N. Webber, R.E. Blankenship, Universality of energy and electron-transfer processes in photosystem-I, Biochemistry 34 (1995) 15512–15522.
[8] E. Schlodder, K. Falkenberg, M. Gergeleit, K. Brettel, Temperature dependence of forward and reverse electron transfer from A1−, the reduced secondary electron acceptor in photosystem I, Biochemistry 37 (1998) 9466–9476.
[9] R. Agalarov, K. Brettel, Temperature dependence of biphasic forward electron transfer from the phylloquinone(s) A1 in photosystem I: only the slower phase is activated, Biochim. Biophys. Acta 1604 (2003) 7–12.
[10] M. Guergova-Kuras, B. Boudreaux, A. Joliot, P. Joliot, K. Redding, Evidence for two active branches for electron transfer in photosystem I, Proc. Natl. Acad. Sci. 98 (2001) 4437–4442.
[11] P. Joliot, A. Joliot, In vivo analysis of the electron transfer within photosystem i: are the two phylloquinones involved? Biochemistry 38 (1999) 11130–11136.
[12] P. Setif, K. Brettel, Forward electron-transfer from phylloquinone-a(1) to iron–sulfur centers in spinach photosystem-I, Biochemistry 32 (1993) 7846–7854.
[13] M. Byrdin, S. Santabarbara, F.F. Gu, W.V. Fairclough, P. Heathcote, K. Redding, F. Rappaport, Assignment of a kinetic component to electron transfer between iron–sulfur clusters F-X and F-A/B of Photosystem I, Biochim. Biophys. Acta Bioenerg. 1757 (2006) 1529–1538.
[14] K. Redding, A. van der Est, The directionality of electron transfer in photosystem I, in: J.H. Golbeck (Ed.)Photosystem I: The Light Driven Plastocyanin:Ferredoxin Oxidoreductase, vol. 24, Springer, Dordrecht, 2006, pp. 413–437.
[15] F. Rappaport, B. Diner, K. Redding, Optical measurements of secondary electron transfer in photosystem I, in: J.H. Golbeck (Ed.)Photosystem I: The Light Driven Plastocyanin:Ferredoxin Oxidoreductase, vol. 24, Springer, Dordrecht, 2006, pp. 223–244.
[16] N. Srinivasan, J.H. Golbeck, Protein–cofactor interactions in bioenergetic complexes: the role of the A(1A) and A(1B) phylloquinones in Photosystem I, Biochim. Biophys. Acta Bioenerg. 1787 (2009) 1057–1088.
[17] S. Santabarbara, P. Heathcote, M.C.W. Evans, Modelling of the electron transfer reactions in Photosystem I by electron tunnelling theory: the phylloquinones bound to the PsaA and the PsaB reaction centre subunits of PS I are almost isoenergetic to the iron–sulfur cluster FX, Biochim. Biophys. Acta Bioenerg. 1708 (2005) 283–310.
[18] H. Ishikita, E.W. Knapp, Redox potential of quinones in both electron transfer branches of photosystem I, J. Biol. Chem. 278 (2003) 52002–52011.
[19] Y.N. Pushkar, J.H. Golbeck, D. Stehlik, H. Zimmermann, Asymmetric hydrogen-bonding of the quinone cofactor in photosystem I probed by C-13-labeled naphthoquinones, J. Phys. Chem. B 108 (2004) 9439–9448.
[20] Y.N. Pushkar, O. Ayzatulin, D. Stehlik, Transient and pulsed EPR study of O-17-substituted methyl-naphthoquinone as radical anion in the A(1) binding site of photosystem I and in frozen solution, Appl. Magn. Reson. 28 (2005) 195–211.
[21] G. Hastings, K.M.P. Bandaranayake, E. Carrion, Time-resolved FTIR difference spectroscopy in combination with specific isotope labeling for the study of A(1), the secondary electron acceptor in photosystem 1, Biophys. J. 94 (2008) 4383–4392.
[22] S. Mula, A. Savitsky, K. Mobius, W. Lubitz, J.H. Golbeck, M.D. Mamedov, A.Y. Semenov, A.v. der Est, Incorporation of a high potential quinone reveals that

electron transfer in Photosystem I becomes highly asymmetric at low temperature, Photochem. Photobiol. Sci. 11 (2012) 946–956.
[23] T.W. Johnson, G. Shen, B. Zybailov, D. Kolling, R. Reategui, S. Beauparlant, I.R. Vassiliev, D.A. Bryant, A.D. Jones, J.H. Golbeck, P.R. Chitnis, Recruitment of a foreign quinone into the A_1 site of photosystem I. I. Genetic and physiological characterization of phylloquinone biosynthetic pathway mutants in Synechocystis sp. pcc 6803, J. Biol. Chem. 275 (2000) 8523–8530.
[24] B. Zybailov, A. van der Est, S.G. Zech, C. Teutloff, T.W. Johnson, G. Shen, R. Bittl, D. Stehlik, P.R. Chitnis, J.H. Golbeck, Recruitment of a foreign quinone into the A(1) site of photosystem I. II. Structural and functional characterization of phylloquinone biosynthetic pathway mutants by electron paramagnetic resonance and electron-nuclear double resonance spectroscopy, J. Biol. Chem. 275 (2000) 8531–8539.
[25] A.Y. Semenov, I.R. Vassiliev, A. van Der Est, M.D. Mamedov, B. Zybailov, G. Shen, D. Stehlik, B.A. Diner, P.R. Chitnis, J.H. Golbeck, Recruitment of a foreign quinone into the A_1 site of photosystem I. Altered kinetics of electron transfer in phylloquinone biosynthetic pathway mutants studied by time-resolved optical, EPR, and electrometric techniques, J. Biol. Chem. 275 (2000) 23429–23438.
[26] V. Sivakumar, R. Wang, G. Hastings, A(1) reduction in intact cyanobacterial photosystem I particles studied by time-resolved step-scan Fourier transform infrared difference spectroscopy and isotope labeling, Biochemistry 44 (2005) 1880–1893.
[27] K. Bandaranayake, V. Sivakumar, R. Wang, G. Hastings, Modeling the A_1 binding site in photosystem I. Density functional theory for the calculation of "anion–neutral" FTIR difference spectra of phylloquinone, Vib. Spectrosc. 42 (2006) 78–87.
[28] K. Bandaranayake, R. Wang, G. Hastings, Modification of the phylloquinone in the A_1 binding site in photosystem i studied using time-resolved FTIR difference spectroscopy and density functional theory, Biochemistry 45 (2006) 4121–4127.
[29] H. Witt, E. Bordignon, D. Carbonera, J.P. Dekker, N. Karapetyan, C. Teutloff, A. Webber, W. Lubitz, E. Schlodder, Species-specific differences of the spectroscopic properties of P700 — analysis of the influence of non-conserved amino acid residues by site-directed mutagenesis of photosystem I from Chlamydomonas reinhardtii, J. Biol. Chem. 278 (2003) 46760–46771.
[30] I.R. Vassiliev, Y.S. Jung, M.D. Mamedov, A.Y. Semenov, J.H. Golbeck, Near-IR absorbance changes and electrogenic reactions in the microsecond-to-second time domain in photosystem I, Biophys. J. 72 (1997) 301–315.
[31] R. Jordan, U. Nessau, E. Schlodder, Charge Recombination Between the Reduced Iron-Sulphur Clusters and $P700^+$, in: G. Garab (Ed.), Photosynthesis, Mechanisms and Effects, Kluwer Academic Publishers, Dordrecht, 1998, pp. 663–666.
[32] K. Brettel, Electron transfer and arrangement of the redox cofactors in photosystem I, Biochim. Biophys. Acta Bioenerg. 1318 (1997) 322–373.
[33] P.V. Warren, J.H. Golbeck, J.T. Warden, Charge recombination between P700+ and A1− occurs directly to the ground state of P700 in a photosystem I core devoid of FX, FB, and FA, Biochemistry 32 (1993) 849–857.
[34] L. Lefebvre-Legendre, F. Rappaport, G. Finazzi, M. Ceol, C. Grivet, G. Hopfgartner, J.-D. Rochaix, Loss of phylloquinone in chlamydomonas affects plastoquinone pool size and photosystem II synthesis, J. Biol. Chem. 282 (2007) 13250–13263.
[35] M.D. McConnell, J.B. Cowgill, P.L. Baker, F. Rappaport, K.E. Redding, Double reduction of plastoquinone to plastoquinol in photosystem 1, Biochemistry 50 (2011) 11034–11046.
[36] V.P. Shinkarev, B. Zybailov, I.R. Vassiliev, J.H. Golbeck, Modeling of the $P700^+$ charge recombination kinetics with phylloquinone and plastoquinone-9 in the A_1 site of photosystem I, Biophys. J. 83 (2002) 2885–2897.
[37] B. Zybailov, Modified Quinone Acceptor in Photosystem I, Ph.D. thesis, Pennsylvania State University, 2003.
[38] J.A. Bautista, F. Rappaport, M. Guergova-Kuras, R.O. Cohen, J.H. Golbeck, J.Y. Wang, D. Beal, B.A. Diner, Biochemical and biophysical characterization of photosystem I from phytoene desaturase and zeta-carotene desaturase deletion mutants of *Synechocystis* Sp. PCC 6803: evidence for PsaA- and PsaB-side electron transport in cyanobacteria, J. Biol. Chem. 280 (2005) 20030–20041.
[39] K.M. Bandaranayake, R. Wang, T.W. Johnson, G. Hastings, Time-resolved FTIR difference spectroscopy for the study of photosystem I particles with plastoquinone-9 occupying the A1 binding site, Biochemistry 45 (2006) 12733–12740.
[40] V. Sivakumar, R. Wang, G. Hastings, A1 reduction in intact cyanobacterial photosystem i particles studied by time-resolved step-scan fourier transform infrared difference spectroscopy and isotope labeling†, Biochemistry 44 (2005) 1880–1893.
[41] G. Hastings, K.M.P. Bandaranayake, Quinone anion bands in A_1^-/A_1 FTIR difference spectra investigated using photosystem I particles with specifically labeled naphthoquinones incorporated into the A_1 binding site, in: J. Allen, E. Gantt, J. Golbeck, B. Osmond (Eds.), Photosynthesis. Energy from the Sun. 14th International Congress on Photosynthesis Research 2007, Springer, 2008, pp. 69–72 (Chapter 12).
[42] C.C. Moser, P.L. Dutton, Engineering protein structure for electron transfer function in photosynthetic reaction centers, Biochim. Biophys. Acta Bioenerg. 1101 (1992) 171–176.
[43] C.C. Page, C.C. Moser, X. Chen, P.L. Dutton, Natural engineering principles of electron tunnelling in biological oxidation–reduction, Nature 402 (1999) 47–52.
[44] A.R. Crofts, S. Rose, Marcus treatment of endergonic reactions: a commentary, Biochim. Biophys. Acta Bioenerg. 1767 (2007) 1228–1232.
[45] R.A. Marcus, On the theory of electron-transfer reactions. VI. Unified treatment for homogeneous and electrode reactions, J. Chem. Phys. 43 (1965) 679–701.
[46] J.J. Hopfield, Electron transfer between biological molecules by thermally activated tunneling, Proc. Natl. Acad. Sci. 71 (1974) 3640–3644.
[47] C.C. Moser, J.M. Keske, K. Warncke, R.S. Farid, P.L. Dutton, Nature of biological electron transfer, Nature 355 (1992) 796–802.
[48] J. Niklas, O. Gopta, B. Epel, W. Lubitz, M.L. Antonkine, Investigation of the stationary and transient A (1) (center dot-) radical in Trp –> Phe mutants of photosystem I, Appl. Magn. Reson. 38 (2010) 187–203.
[49] C.C. Moser, P.L. Dutton, Application of Marcus theory to photosystem i electron transfer, in: G. Golbeck (Ed.), Photosystem I: The Light Driven Plastocyanin: Ferredoxin Oxidoreductase, Springer, Dordrecht, 2006, pp. 583–594.
[50] K. Brettel, W. Leibl, Electron transfer in photosystem I, Biochim. Biophys. Acta Bioenerg. 1507 (2001) 100–114.
[51] V. Ptushenko, D. Cherepanov, L. Krishtalik, A. Semenov, Semi-continuum electrostatic calculations of redox potentials in photosystem I, Photosynth. Res. 97 (2008) 55–74.
[52] S. Santabarbara, K. Reifschneider, A. Jasaitis, F. Gu, G. Agostini, D. Carbonera, F. Rappaport, K.E. Redding, Interquinone electron transfer in photosystem i as evidenced by altering the hydrogen bond strength to the phylloquinone(s), J. Phys. Chem. B 114 (2010) 9300–9312.
[53] M. Iwaki, S. Itoh, Reaction of reconstituted acceptor quinone and dynamic equilibration of electron transfer in the photosystem i reaction center, Plant Cell Physiol. 35 (1994) 983–993.
[54] P. Sétif, P. Mathis, T. Vänngård, Photosystem I photochemistry at low temperature. Heterogeneity in pathways for electron transfer to the secondary acceptors and for recombination processes, Biochim. Biophys. Acta Bioenerg. 767 (1984) 404–414.
[55] S. Santabarbara, I. Kuprov, O. Poluektov, A. Casal, C.A. Russell, S. Purton, M.C.W. Evans, Directionality of electron-transfer reactions in photosystem i of prokaryotes: universality of the bidirectional electron-transfer model, J. Phys. Chem. B 114 (2010) 15158–15171.
[56] S. Santabarbara, I. Kuprov, P.J. Hore, A. Casal, P. Heathcote, M.C.W. Evans, Analysis of the spin-polarized electron spin echo of the [P700 + A1−] radical pair of photosystem I indicates that both reaction center subunits are competent in electron transfer in cyanobacteria, green algae, and higher plants†, Biochemistry 45 (2006) 7389–7403.
[57] A. Ogrodnik, W. Keupp, M. Volk, G. Aumeier, M.E. Michel-Beyerle, Inhomogeneity of radical pair energies in photosynthetic reaction centers revealed by differences in recombination dynamics of P + HA− when detected in delayed emission and in absorption, J. Phys. Chem. 98 (1994) 3432–3439.
[58] R.A. Marcus, N. Sutin, Electron transfers in chemistry and biology, Biochim. Biophys. Acta Rev. Bioenerg. 811 (1985) 265–322.